

Imaging ionospheric inhomogeneities using spaceborne synthetic aperture radar

Xiaoqing Pi,¹ Anthony Freeman,¹ Bruce Chapman,¹ Paul Rosen,¹ and Zhenhong Li²

Received 4 November 2010; revised 20 January 2011; accepted 25 January 2011; published 8 April 2011.

[1] We present a technique and results of 2-D imaging of Faraday rotation and total electron content using spaceborne *L* band polarimetric synthetic aperture radar (PolSAR). The results are obtained by processing PolSAR data collected using the Phased Array type L-band Synthetic Aperture Radar (PALSAR) on board the Advanced Land Observation Satellite. Distinguished ionospheric inhomogeneities are captured in 2-D images from space with relatively high resolutions of hundreds of meters to a couple of kilometers in auroral-, middle-, and low-latitude regions. The observed phenomena include aurora-associated ionospheric enhancement arcs, the middle-latitude trough, traveling ionospheric disturbances, and plasma bubbles, as well as ionospheric irregularities. These demonstrate a new capability of spaceborne synthetic aperture radar that will not only provide measurements to correction of ionospheric effects in Earth science imagery but also significantly benefit ionospheric studies.

Citation: Pi, X., A. Freeman, B. Chapman, P. Rosen, and Z. Li (2011), Imaging ionospheric inhomogeneities using spaceborne synthetic aperture radar, *J. Geophys. Res.*, 116, A04303, doi:10.1029/2010JA016267.

1. Introduction

[2] It is well known that the ionosphere as a media of radio propagation causes additional time delay, phase advance, and polarization changes in radio signals that traverse the ionosphere. These effects become appreciable at *L* band and lower frequencies owing to the dispersive nature of the ionosphere. As spaceborne *L* band synthetic aperture radars (SARs) are applied to remote sensing of Earth's surface deformations, biomass, and cryospheric dynamics, use of SAR to measure the ionosphere also becomes desirable. This is because such measurements not only makes it possible to detect and correct the ionospheric effects in Earth science remote sensing imagery, but also significantly benefit ionospheric studies.

[3] For example, if horizontal gradient or curved structures of ionospheric density are present in a satellite path, ionospheric-induced phase and polarization changes in the remote sensing radio signals can occur inhomogeneously in a radar scene. The effects can cause distortions in interferograms of *L* band or lower-frequency interferometric SAR (InSAR) images [e.g., *Ishimaru et al.*, 1999; *Liu et al.*, 2003; *Freeman*, 2004; *Chapin et al.*, 2006; *Pi and Chan*, 2006; *Meyer and Nicoll*, 2008; *Shimada et al.*, 2008; *Freeman et al.*, 2008; *Pi et al.*, 2008; *Rosen et al.*, 2009;], which must be removed to obtain quality Earth science images. Further if plasma irregularities are present, the

well-known ionospheric scintillation effects can occur and cause random changes in signal power, phase, and polarization. These effects can cause artifacts in InSAR images and must be identified. Measuring the ionosphere using satellite-based SAR would make it possible to provide needed data to correct or identify the ionospheric effects. In addition, satellite-based SAR techniques would have a great potential for 2-D ionospheric imaging from space. The major advantages include that such imaging will have relatively high resolution, can be conducted globally, and is not susceptible to weather conditions and various light sources that can hinder optical imaging.

[4] A key to success of ionospheric correction in SAR imaging is spatial resolution of the ionospheric imaging. In the detection and correction, it is required to resolve ionospheric structures presumably down to kilometers or sub-kilometer scales. In the ionospheric measurement respect, imaging from space at such spatial resolutions would fill the gap of existing ionospheric observation capabilities. On smaller scales, ionospheric density distribution varies smoothly except for plasma irregularities and plasma bubbles.

[5] Here we review and summarize some results that have been presented by us in conferences since 2008. We present a technique of imaging the ionosphere using polarimetric measurements of spaceborne SAR, and show imaging results of ionospheric inhomogeneities in high-, middle-, and low-latitude regions. The SAR data presented in this work are collected using the Phased Array type L-band Synthetic Aperture Radar (PALSAR) on board the Japanese Advanced Land Observation Satellite (ALOS; see http://www.jaxa.jp/projects/sat/alos/index_e.html). Ionospheric total electron content (TEC) measurements derived from GPS data collected using the International GPS Service network

¹Jet Propulsion Laboratory, California Institute of Technology, Pasadena, California, USA.

²Department of Geographical and Earth Sciences, University of Glasgow, Glasgow, UK.

and the GPS Earth Observation Network (GEONET) in Japan are also presented to verify the SAR observations.

[6] Using PALSAR polarimetric data, *Meyer and Nicoll* [2008] and *Pi et al.* [2008] have previously obtained FR images in the polar region, which show enhanced FR bands and the effects on InSAR imagery. *Rosen et al.* [2009] have applied a split-spectrum technique to the measurement of differential TEC and the correction to satellite repeat-pass InSAR imagery in the polar region. The technique utilizes the limited bandwidth (14 to 28 MHz depending on the operation mode) of the PALSAR data to construct phase images at the two bands to derive the differential TEC. *Shimada et al.* [2008] have reported anomalies (streaks) in the PALSAR land images and pointed out that the anomalies are due to ionospheric irregularities. In this work, we focus on ionospheric imaging without including the effects on land images to limit the length of this paper. Our imaging results are organized in such a way that manifests distinguished ionospheric phenomena at high, middle, and low latitudes. These phenomena include TEC enhancement associated with aurora arcs, the middle-latitude ionospheric trough, traveling ionospheric disturbances (TIDs), plasma bubbles and ionospheric irregularities that cause ionospheric scintillation in the L band SAR signals. We start with a review of some fundamentals of ionospheric effects on radio signals in section 2, which is followed by a description of measuring Faraday rotation using polarimetric SAR (section 3). Examples of 2-D images of Faraday rotation and TEC derived from PALSAR polarimetric data are presented in section 4 to show ionospheric inhomogeneities at high, middle, and low latitudes. Spatial resolutions of SAR ionospheric imaging are discussed in section 5. Section 6 summarizes our conclusions.

2. Ionospheric Effects on Radio Signals

[7] In this section, some fundamental ionospheric effects on radio propagation are briefly reviewed that help to assess the ionospheric imaging results to be presented in section 4. The formula of ionospheric refractive index is one of the fundamental equations and often referred to the Appleton-Lassen formula or Appleton-Hartree formula, named after the British and German scientists who derived it in 1920s and 1930s. In a magnetized, anisotropic, and ionized media, a radio wave splits into the ordinary and extraordinary waves in general that have different phase velocities. The corresponding refractive index is a function of electron density, the ambient magnetic field, and the frequency of the radio signal. Its full expression is referred to readily accessible references [e.g., *Budden*, 1985; *Davis*, 1990]. A simplified form (neglecting higher-order terms) can be expressed as

$$\mu_{O,E} \approx 1 - \frac{1}{2}X(1 \mp Y), \quad (1)$$

where subscripts O and E denote the ordinary and extraordinary waves, respectively. Parameter $X = \left(\frac{\omega_p}{\omega}\right)^2$, $\omega_p = \left(\frac{n_e e^2}{\epsilon_0 m_e}\right)^{1/2}$ is the angular plasma frequency, n_e is electron density, e is the elementary charge, ϵ_0 is the permittivity of free space, m_e is the electron mass, and $\omega = 2\pi f$ is angular radio frequency. $Y = \frac{\omega_H}{\omega}$, $\omega_H = \frac{|e|B}{m_e}$ is the electron gyro fre-

quency, and B denotes the magnitude of ambient magnetic field. The upper ($-$) and lower ($+$) signs apply to the ordinary and extraordinary waves, respectively.

[8] Michael Faraday discovered in 1845 that as a signal propagates through a magnetized media, its polarization rotates an angle with respect to the original orientation. The phenomenon is characterized as Faraday rotation, and results from different speeds and opposite directions of polarization rotations. The angle of the rotation can be derived by integration of half the phase difference between the ordinary and extraordinary waves along the propagation distance; that is,

$$\Omega = \int \frac{1}{2} \frac{\omega}{c} (\mu_O - \mu_E) ds, \quad (2)$$

where c is the speed of light and ds is the incremental length along the raypath, assuming that the wave propagates in the direction of magnetic field. In general one can obtain the Faraday rotation integration as

$$\Omega = \frac{|e|^3}{8\pi^2 c \epsilon_0 m_e^2 f^2} \int n_e B \cos \theta ds = \frac{2.365 \times 10^4}{f^2} \int n_e B \cos \theta ds, \quad (3)$$

where θ is the angle between the vectors of radio wave and ambient magnetic field, and the formula is in MKS unit.

[9] For typical spaceborne SAR observation geometries, $\cos \theta$ varies little along the radio raypaths within a radar scene and B varies monotonically in altitude dimension. Fluctuations in the magnetic field caused by ionospheric and magnetospheric currents can be neglected since they are usually less than 1%, or a few percent in the polar region under severe magnetic storms. Thus the product $B \cos \theta$ can be replaced with a mean or median value along the raypath and taken out from the integration. In SAR practice Faraday rotation can then be computed as

$$\Omega = \frac{2.365 \times 10^4}{f^2} \langle B \cos \theta \rangle \text{TEC}. \quad (4)$$

where $\text{TEC} = \int n_e ds$ denotes total electron content along the radio raypath between the transmitter and receiver. Using this equation, TEC can be derived from FR measurements by specifying $\langle B \cos \theta \rangle$.

[10] Similarly, ionospheric-induced phase change can also be derived. For an L band signal, the magnetic effect is so small that the refractive index can be further simplified for most applications by neglecting the Y term in equation (1); that is,

$$\mu \approx 1 - \frac{1}{2}X. \quad (5)$$

As the signal propagates in the ionosphere, its phase change with respect to the initial phase in terms of traveled distance is

$$\begin{aligned} \phi - \phi_0 &= \int k ds = \int \frac{\omega}{v_p} ds = \frac{\omega}{c} \int \mu ds \approx \frac{\omega}{c} \int \left(1 - \frac{1}{2}X\right) ds \\ &= \phi_c + \phi_I, \end{aligned} \quad (6)$$

$$\phi_I = -\frac{\omega}{2c} \int X ds = -\frac{2\pi}{c} \frac{e^2}{8\pi^2 \epsilon_0 m_e f} \int n_e ds = -\frac{8.45 \times 10^{-7}}{f} \text{TEC}, \quad (7)$$

where ϕ_0 is the initial phase, ϕ_c is the phase change as the signal propagates in vacuum, and v_p is the phase velocity. The negative sign in front of the ionospheric-induced phase change (ϕ_I) indicates that there is less phase change as the signal propagates through the ionosphere than through vacuum for a same distance. Its corresponding absolute phase path in units of distance is

$$d_I = \frac{40.3}{f^2} \text{TEC} \quad (8)$$

It is noted that both phase and Faraday rotation effects are proportional to TEC. To compare the two effects, one can compute the ratio of ϕ_I to Ω ; that is,

$$\gamma_\phi = \frac{\phi}{\Omega} = 3.574 \times 10^{-11} \frac{f}{\langle B \cos \theta \rangle}. \quad (9)$$

Note that the ratio depends on radio frequency. For example, assuming an L band signal at $f = 1270$ MHz, $B = 0.4 \times 10^{-4}$ Tesla, $\theta = 45^\circ$, one can obtain $\gamma_\phi = 1604.8$. For a P band signal at $f = 400$ MHz and the same magnetic field strength and propagation geometry, $\gamma_\phi = 505.4$. Another useful parameter is the ratio of d_I to Ω ; that is,

$$\begin{aligned} \gamma_d = \frac{d_I}{\Omega} &= 1.7 \times 10^{-3} \frac{1}{\langle B \cos \theta \rangle} \quad [\text{m/rad}] \\ &= 2.974 \times 10^{-5} \frac{1}{\langle B \cos \theta \rangle} \quad [\text{m/deg}]. \end{aligned} \quad (10)$$

The parameter γ_d measures ionospheric-induced signal delay in meters for every degree of Faraday rotation. Using the above magnetic field strength and propagation geometry, one can obtain $\gamma_d = 1.05$ m/deg. For observation geometry of θ close to 90° , which can occur near the magnetic equator, γ_d becomes large since the factor $\cos \theta$ becomes small.

3. Measuring Faraday Rotation Using Polarimetric SAR

[11] For a SAR system performing full polarimetric measurements, *Freeman* [2004] described the effects of Faraday rotation on the radar polarimetry and the required system calibration. Here we briefly summarize the fundamental equations of radar polarimetric measurements as follows, which leads to a method of deriving Faraday rotation. For a polarimetric SAR transmitting and measuring linear horizontal (H) and vertical (V) polarizations, the measured scattering matrix (\mathbf{M}) can be expressed as

$$\begin{aligned} \begin{pmatrix} M_{hh} & M_{vh} \\ M_{hv} & M_{vv} \end{pmatrix} &= A(r, \theta) e^{j\phi} \begin{pmatrix} 1 & \delta_2 \\ \delta_1 & 1 \end{pmatrix} \begin{pmatrix} 1 & 0 \\ 0 & f_1 \end{pmatrix} \\ &\cdot \begin{pmatrix} \cos \Omega & \sin \Omega \\ -\sin \Omega & \cos \Omega \end{pmatrix} \begin{pmatrix} S_{hh} & S_{vh} \\ S_{hv} & S_{vv} \end{pmatrix} \\ &\cdot \begin{pmatrix} \cos \Omega & \sin \Omega \\ -\sin \Omega & \cos \Omega \end{pmatrix} \begin{pmatrix} 1 & 0 \\ 0 & f_2 \end{pmatrix} \begin{pmatrix} 1 & \delta_3 \\ \delta_4 & 1 \end{pmatrix} \\ &+ \begin{pmatrix} N_{hh} & N_{vh} \\ N_{hv} & N_{vv} \end{pmatrix}, \end{aligned} \quad (11)$$

or

$$\mathbf{M} = A e^{j\phi} \mathbf{R}^T \mathbf{R}_F \mathbf{S} \mathbf{R}_F \mathbf{T} + \mathbf{N}, \quad (12)$$

where \mathbf{S} is the scattering matrix and \mathbf{R}_F is the one-way Faraday rotation matrix. \mathbf{T} and \mathbf{R}^T are the transmit distortion matrix and transpose of the receive distortion matrix, respectively, both of which include cross-talk (δ terms) and channel amplitude and phase imbalance (f_1 and f_2). \mathbf{N} is the additive noise matrix. A represents the overall gain of the radar system, which is a function of range (r) and elevation angle (θ). ϕ represents the round-trip phase delay and system-dependent phase effects.

[12] The system distortion can be calibrated using traditional methods if the Faraday rotation effect is zero or can be neglected. We have also developed a method to perform the system calibration with polarimetric measurements under conditions of limited Faraday rotation effect [*Freeman et al.*, 2009]. Briefly, considering a condition of small Faraday rotation (i.e., $\sin \theta \approx \theta$ and $\cos \theta \approx 1$), equation (11) can be approximately expressed as

$$\begin{aligned} \begin{pmatrix} M_{hh} & M_{vh} \\ M_{hv} & M_{vv} \end{pmatrix} &= A(r, \theta) e^{j\phi} \begin{pmatrix} 1 & \delta_2 + \Omega \\ \delta_1 - \Omega f_1 & f_1 \end{pmatrix} \begin{pmatrix} S_{hh} & S_{vh} \\ S_{hv} & S_{vv} \end{pmatrix} \\ &\cdot \begin{pmatrix} 1 & \delta_3 + \Omega f_2 \\ \delta_4 - \Omega & f_2 \end{pmatrix} + \mathbf{N}. \end{aligned} \quad (13)$$

We rewrite this equation to the following:

$$\begin{aligned} \begin{pmatrix} M_{hh} & M_{vh} \\ M_{hv} & M_{vv} \end{pmatrix} &= A(r, \theta) e^{j\phi} \begin{pmatrix} 1 & \delta'_2 \\ \delta'_1 & f_1 \end{pmatrix} \begin{pmatrix} S_{hh} & S_{vh} \\ S_{hv} & S_{vv} \end{pmatrix} \\ &\cdot \begin{pmatrix} 1 & \delta'_3 \\ \delta'_4 & f_2 \end{pmatrix} + \mathbf{N}, \end{aligned} \quad (14)$$

where $\delta'_1 = \delta_1 - \Omega f_1$, $\delta'_2 = \delta_2 + \Omega$, $\delta'_3 = \delta_3 + \Omega f_2$, and $\delta'_4 = \delta_4 - \Omega$. In addition, a parameter $F = \frac{f_1}{f_2}$ is introduced to represent the ratio of receive and transmit imbalances. Equation (14) now is in a form that δ'_1 , δ'_2 , δ'_3 , δ'_4 , and F become the new distortion parameters. Such a system can be calibrated by applying traditional methods such as *Quegan's* [1994] method as if the Faraday rotation effect is neglected. As the new parameters are solved for, δ_1 , δ_2 , f_1 , f_2 and Ω can be derived. We have applied our method to an estimation of the PALSAR polarimetric system calibration parameters, which is performed using a series of PALSAR data sets without corner reflectors [*Freeman et al.*, 2009]. The estimation shows consistent results with what JAXA obtained using *Quegan's* method with a corner reflector deployed in the Amazon, where the Faraday rotation is minimized owing to the geometries of radar beams and the ambient geomagnetic field.

[13] After the system calibration, the measurement equation can be formed as

$$\mathbf{M} = \mathbf{R}_F \mathbf{S} \mathbf{R}_F. \quad (15)$$

where \mathbf{M} is calibrated polarimetric measurement matrix, and \mathbf{N} is neglected which can be minimized in data processing using filtering or smoothing techniques. Several methods have been developed to solve for FR effects and to remove the effects from the scattering measurements. Here we

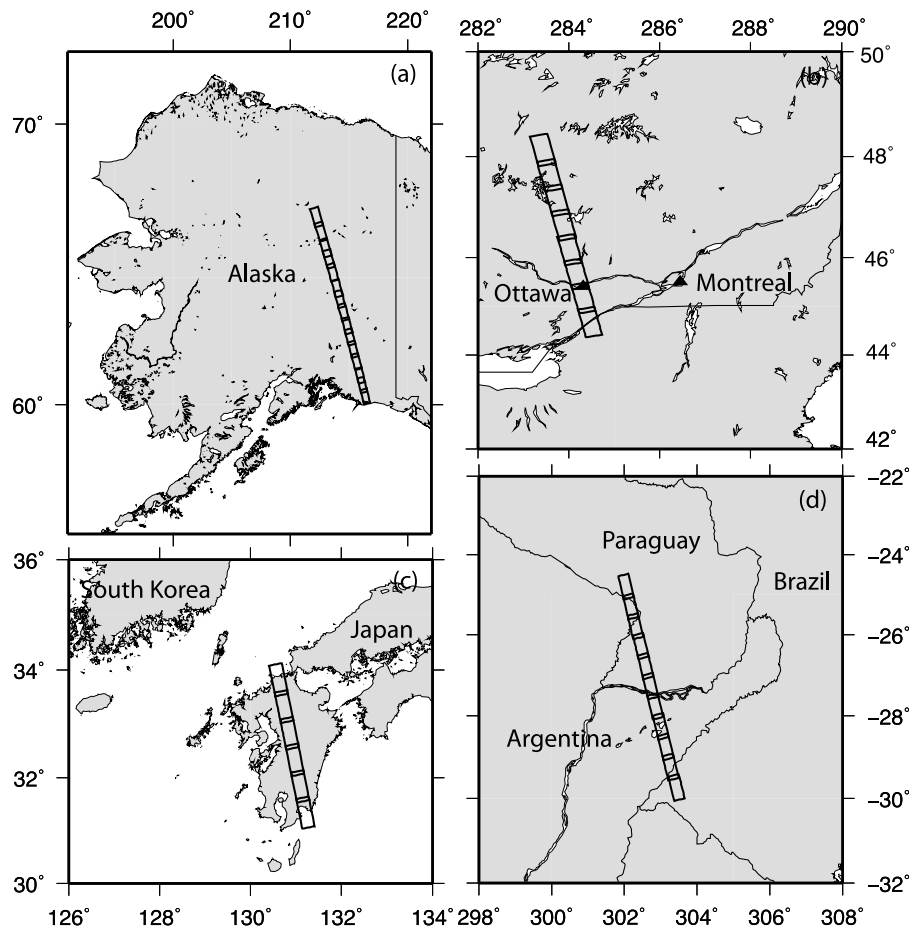


Figure 1. The coverage and map projection of PALSAR observation ground tracks presented in this work for imaging ionospheric inhomogeneities at (a) high, (b and c) middle, and (d) low latitudes. All observations were made along ascending orbit tracks from lower to higher latitudes. The projection of radar observation range direction to the ground is in the cross-track direction (to the right).

introduce an approach proposed by *Bickel and Bates* [1965], who applied a simple transformation as follows:

$$\begin{bmatrix} Z_{11} & Z_{12} \\ Z_{21} & Z_{22} \end{bmatrix} = \begin{bmatrix} 1 & j \\ j & 1 \end{bmatrix} \begin{bmatrix} M_{hh} & M_{vh} \\ M_{hv} & M_{vv} \end{bmatrix} \begin{bmatrix} 1 & j \\ j & 1 \end{bmatrix}. \quad (16)$$

With an assumption of reciprocal scatterer ($S_{hv} = S_{vh}$), one can solve for Faraday rotation as

$$\Omega = \frac{1}{4} \arg(Z_{12}Z_{21}^*). \quad (17)$$

4. Ionospheric Variations Imaged in Different Latitude Regions

[14] The 2-D ionospheric imaging technique described in section 3 is applicable for a system operating at L band and lower frequencies since the Faraday rotation effect becomes appreciable at these frequencies. The Phased Array type L-band Synthetic Aperture Radar (PALSAR; $f_0 = 1270$ MHz) on board the Advanced Land Observation Satellite (ALOS) is such a system. ALOS is an Earth science mission launched by the Japan Aerospace Exploration Agency (JAXA) on 24 January 2006, orbiting at about 692 km altitude Sun-

synchronously ($\sim 1000/2200$ LT). PALSAR has operated primarily on finebeam and ScanSAR modes since the launch of ALOS. In addition, it has also operated experimentally to collect polarimetric data in different regions of the world.

[15] In this section, we will present 2-D images of slant-range Faraday rotation (FR) derived from polarimetric data that are collected using PALSAR from polar, midlatitude, and equatorial regions. Figure 1 gives the coverage and map projection of PALSAR observation ground tracks to be presented in this work. Before ionospheric processing, full polarimetric data (HH, HV, VH, and VV) are calibrated by JAXA for radiometry, phase, cross-talk and channel imbalance. The PALSAR product calibration conducted by JAXA and its applications are referred to *Shimada et al.* [2009]. A typical calibrated single-look complex (SLC) polarimetric data for a PALSAR image scene is composed of 1248×18432 pixels in range and azimuth dimensions, and the sampling spacing is about 9.369 and 3.557 m. These correspond to about 23.128 and 3.557 m on average on the ground in cross- and along-track dimensions, respectively. The FR processing as described in the section 3 is applied to the calibrated SLC data to derive FR images. A FR image derived from SLC data is often noisy and can be contaminated by ground topographic features. Thus image smoothing or

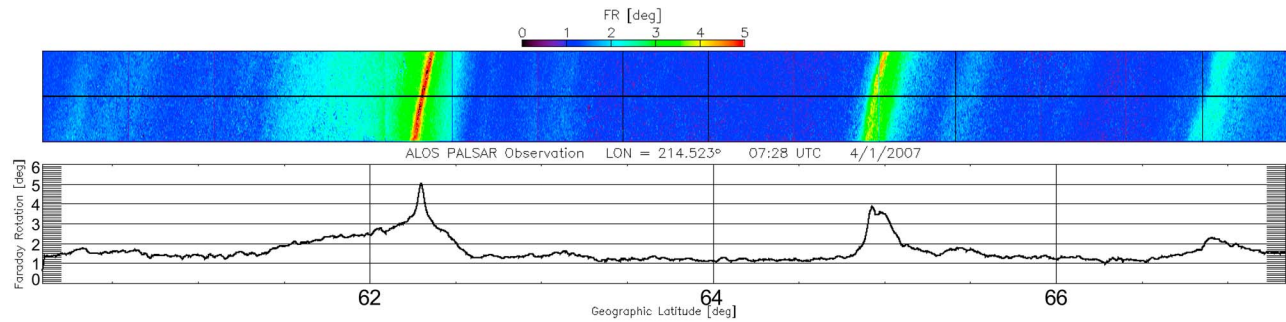


Figure 2. (top) Image strip of line-of-sight Faraday rotation (FR) derived from PALSAR observations over Alaska on 1 April 2007. The strip covers about $30 \times 900 \text{ km}^2$ extending from about $(216.28^\circ\text{E}, 60.008^\circ\text{N})$ to $(212.335^\circ\text{E}, 67.432^\circ\text{N})$ along the satellite ascending orbit track (see Figure 1a). (bottom) The 1-D FR values extracted from the image center as indicated by a line. The spaceborne synthetic aperture radar data present remarkable FR enhancement arcs, which are due to total electron content enhancements associated with auroral activities under disturbed space weather conditions.

filtering is required to remove such noise. In our analysis a boxcar smoothing is applied at least that replaces FR value for each pixel with an average of a number of surrounding data points. The number of data points used in an average depends on the degree of noise. A bandpass or lowpass filter may also be applied when necessary and data outliers, if identified, are replaced by interpolated values.

[16] Corresponding TEC images will also be presented. As indicated in equation (4), deriving TEC image from FR involves the ambient geomagnetic field, including its magnitude and orientation. In our analysis we use International

Geomagnetic Reference Field (IGRF), an empirical model which includes the main core field and external fields due to ionospheric and magnetospheric currents. Horizontally, the modeled magnetic field does not vary much within a typical radar scene, which is about $\sim 30 \times 60 \text{ km}^2$ for the polarimetric mode. However, the magnitude of magnetic field varies substantially with altitude. The vertical variation arises mostly from the main field which is continuous and approximately follows a dipole field in near Earth space. Thus, in computing TEC from FR, equation (4) is used in which the integration is replaced with a mean value

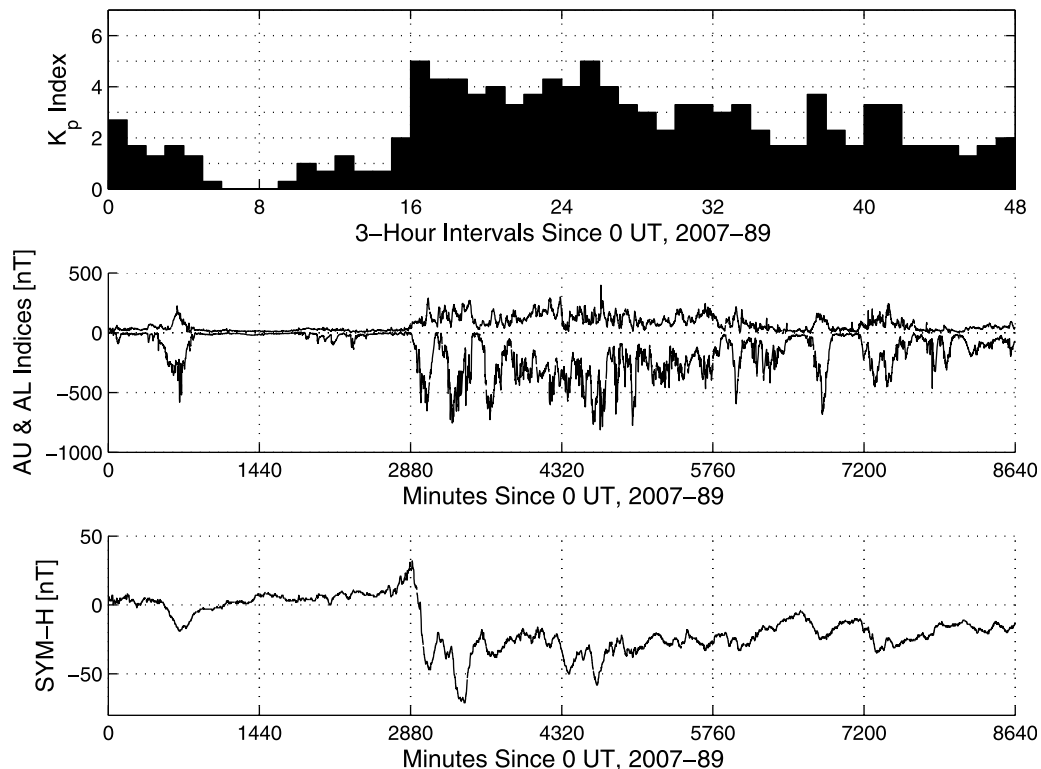


Figure 3. Geomagnetic indices for (top) K_p , (middle) auroral electrojet, and (bottom) SYM-H showing a geomagnetic storm during 1–2 April 2007 (days of year 91 and 92; the plotted data start at the beginning of 30 March 2007, day of year 89).

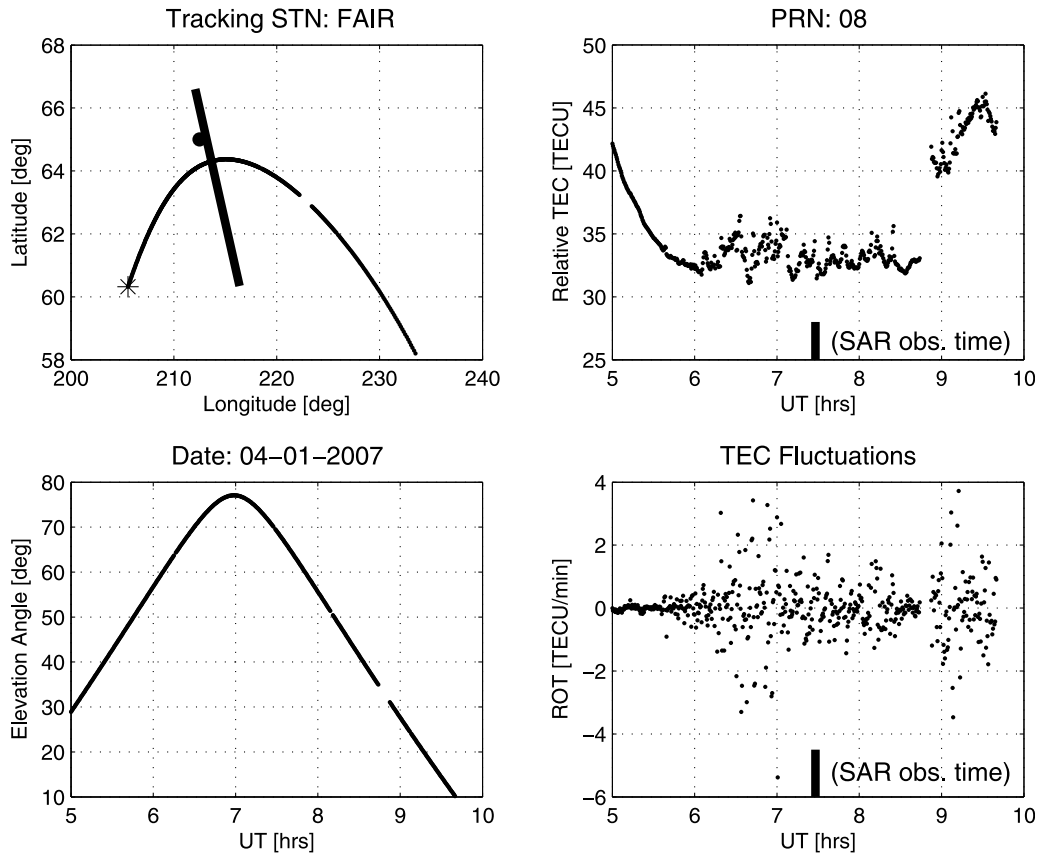


Figure 4. Relative total electron content (TEC) and rate of TEC (ROT) data collected using a dual-frequency GPS receiver in Fairbanks, Alaska. The observing site is marked by the large solid circle. The GPS observations on 1 April 2007 from a receiver-to-satellite (pseudorandom number (PRN) = 8) radio link show perturbed TEC structures in the region adjacent to the Advanced Land Observation Satellite pass at about 0747 UT. The asterisk indicates the starting point of GPS track at 0500 UT. The PALSAR observation track from lower to higher latitudes and the time of PALSAR observation are also marked.

($B \cos \theta$) for a pixel. In addition, interpolations are also applied to the horizontal dimensions to reduce computation.

4.1. TEC Enhancements Associated With Aurora Activities

[17] Figure 2 (top) presents a FR image strip along an ALOS ascending pass over Alaska. In Figure 2 (bottom) the along-track direction is from lower to higher latitudes (see also Figure 1a). The included polarimetric SAR (PolSAR) observations were made between about 0727 and 0729 UT on 1 April 2007. The radar images extend from about (216.28°E, 60.008°N) to (212.335°E, 67.432°N), referring to Figure 1a, covering an area of about 30×900 km². In deriving the 2-D image, a 2-D smoothing is applied which takes an average of surrounding 21×41 points centered at the pixel of interest. This reduces the image resolutions to about 486 and 146 m in cross- and along-track dimensions, respectively. A sample of 1-D FR extracted from the image center is also plotted (Figure 2, bottom).

[18] The remarkable patterns shown in the 2- and 1-D data are enhanced FR arcs. These arcs are all aligned in an approximately same direction. The magnitude and width of individual arcs are different. There are diffused enhance-

ments around the brightest arc at $\sim 62.25^\circ$ N latitude, and the range of diffusive feature on each side of the arc can be different, some showing more on the lower-latitude side such as the arc mentioned above and some on the opposite side such as the one near $\sim 64.9^\circ$ N. Even weak arcs can be identified easily near 60.4° N, 60.6° N, 63.2° N, 65.4° N, and 66° N latitudes. Examining the orientations of the arcs and compare them with the IGRF geomagnetic field, we find that the arcs are approximately aligned with the contours of magnetic inclination angles. These arc features lead us to speculate that they are associated with aurora activities in which charged particle precipitation can cause aurora arcs and TEC enhancements as seen in the FR images.

[19] It is well known that the nominal auroral zone in the northern hemisphere is around about 65° N magnetic latitude, and aurora activities significantly increase during geomagnetic storms under disturbed space weather conditions. Checking the space weather and geophysical conditions, we learnt that there was a geomagnetic storm occurred on 1 April 2007. Figure 3 shows geomagnetic index data indicating increased auroral electrojet activities at the time of the ALOS pass under the context of global geomagnetic activities. In addition, we also examined GPS data collected

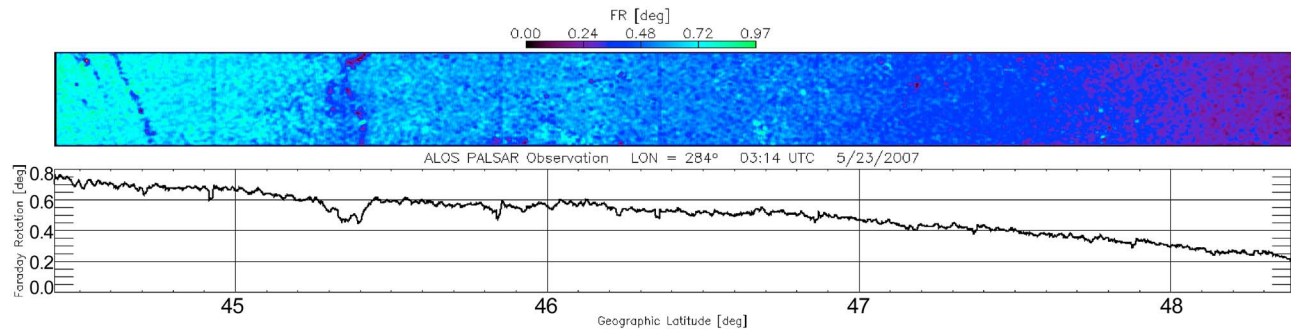


Figure 5. (top) The 2- and 1-D Faraday rotation (FR) derived from polarimetric data taken by PALSAR in an ascending orbit pass (approximately northward; see Figure 1b) over North America on 23 May 2007. (bottom) Mean values of the FR image in cross-track dimension along the observation track. The synthetic aperture radar observations present a distinguished gradient feature in FR near the midlatitude ionospheric trough.

from a NASA station in Fairbanks, Alaska, as part of the International GPS Service (IGS) network. From GPS dual-frequency phase measurements, one can derive TEC and rate of TEC (ROT) change or rate of TEC index (ROTI) [e.g., *Pi et al.*, 1997], the latter being an indicator of irregular ionospheric structures. Figure 4 presents such ionospheric measurements taken from a GPS receiver-to-satellite radio link (the pseudorandom number (PRN) of the GPS satellite is 8) during the ALOS pass. The GPS data show structured TEC enhancements in the adjacent regions of ALOS pass at the time and associated ionospheric irregularities. The magnetic and GPS measurements as well as the characteristics of PALSAR FR images indicate that the enhanced FR arcs are associated with auroral arcs during the geomagnetic storm.

4.2. Ionospheric Gradient in the Midlatitude Trough Region

[20] The midlatitude ionospheric trough is a region of depleted electron density nominally near the 60° magnetic latitude [e.g., *Muldrew*, 1965; *Liszka*, 1965]. The region is a footprint of the plasmopause down to the ionosphere along the magnetic field line. It is the boundary between plasma

convection driven by the coupling of magnetosphere and ionosphere in the polar region and ionospheric corotation with Earth at lower latitudes. The formation of the trough is believed to be due to a combined effect of convection electric field in the polar region and local chemical recombination [e.g., *Schunk et al.*, 1975; *Spiro et al.*, 1978], and the former can be significantly enhanced during disturbed space weather events. The characteristics of the trough can be described as: (1) its width can be a few degrees wide in latitude; (2) the latitudinal gradient of electron density around the trough is sharp; (3) it extends in the magnetic longitude direction; and (4) the trough can move to lower latitudes under disturbed space weather conditions.

[21] Figure 5 presents FR measurements in the same layout as in Figure 2 but for a North America region near 284°E longitude between 44.4°N and 48.4°N geographic latitudes. The corresponding invariant magnetic latitudes are 55.3°N and 59°N , and the northern edge is near the nominal region of the middle-latitude trough. The measurements were taken on 23 May 2007 for an ascending pass at about 0314 UT, covering about $\sim 30 \times 480 \text{ km}^2$. The image resolution is reduced to about 486 and 146 m after applying the smoothing. The image shows clear FR gradient in the lati-

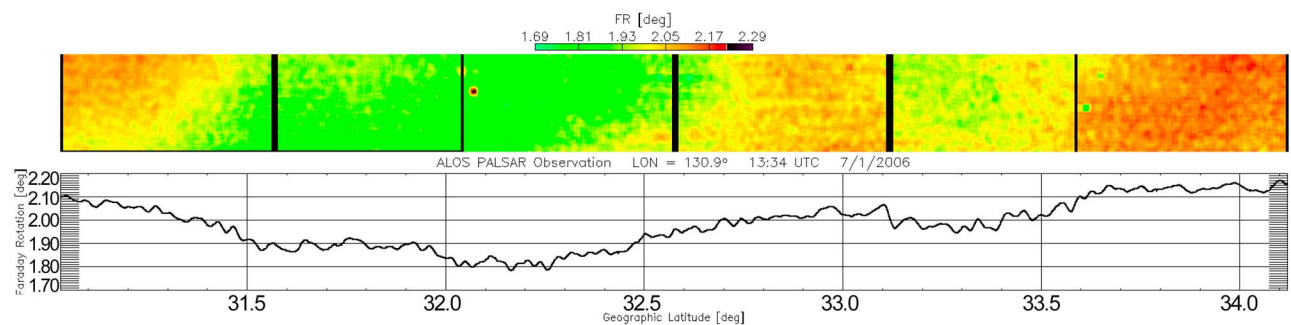


Figure 6. (top) The 2- and 1-D Faraday rotation (FR) derived from polarimetric data taken by PALSAR on board ALOS in an ascending orbit pass (from lower to higher latitudes; see Figure 1c) over Japan on 1 July 2006. (bottom) The 1-D FR is extracted from the image center (similarly as in Figure 2). The synthetic aperture radar observations show wave-like perturbations in FR or total electron content associated with traveling ionospheric disturbances in the region during the evening.

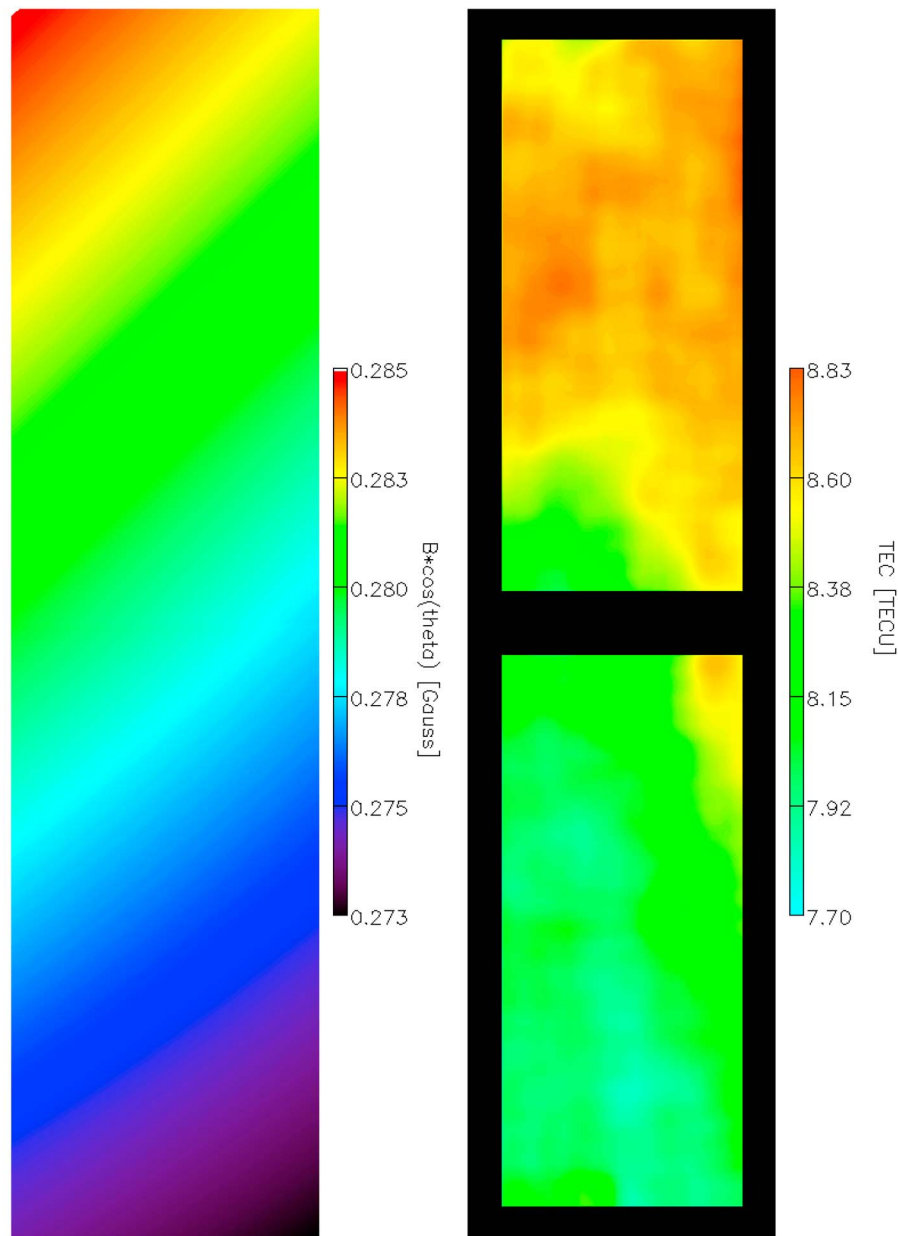


Figure 7. (left) Factor $\langle B \cos \theta \rangle$ is computed using International Geomagnetic Reference Field with the ALOS spacecraft attitude information as well as observation geometry. (right) Total electron content (TEC) is converted from the Faraday rotation images shown in Figure 6 (around 32.6°N).

tude direction, and the gradient becomes steeper at the higher-latitude end. The ratio of FR/latitude reaches about 0.24 near the northern end where the trough is nominally located. This gradient increase must be due to TEC change in the region since horizontal variations of the ambient geomagnetic field and radar observation look angle are negligible within the radar scenes. We also notice that there are curved depletion strips across the FR image such as the one near 45.3°N latitude. Similar strips appear at about 44.5°N and 44.7°N . Examining the surface targets, we identified that these depletions are results of rivers and a lake in Ottawa and Rockville, Canada, respectively, which contaminate the Faraday rotation measurements.

4.3. Midlatitude Traveling Ionospheric Disturbances

[22] Figure 6 shows 2-D FR derived from polarimetric data for six radar images collected over an ascending pass of ALOS over Japan at about 1334 UT on 1 July 2006. The resolution of each image is reduced to about 2 km in each dimension after applying smoothing to remove noise. The black edges in each image are due to setting zero to non-smoothed values on the edges, which become more apparent as more data samples are used in smoothing for each pixel. The pronounced feature in this case is a wave-like structure in the intensity of FR, such as a wide peak near 33°N (refer to 1-D plot in Figure 6 (bottom)) that is accompanied by troughs on two sides. Roughly measuring distance between

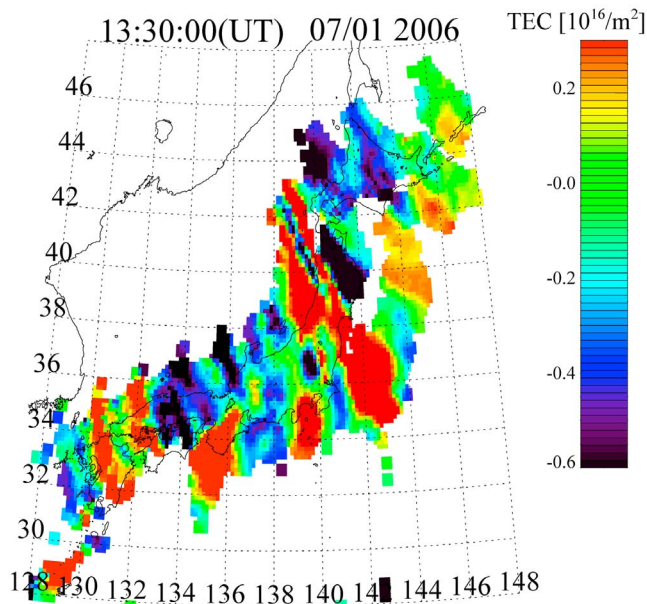


Figure 8. Traveling ionospheric disturbances in total electron content (TEC) perturbations were observed on 1 July 2006 using the GPS Earth Observation Network of Japan (image courtesy of Akinori Saito, Kyoto University). The PALSAR pass at the same time is referred to (see Figure 1) in a region enclosed by 130–132°E and 31–34°N.

the FR peak and trough, we estimate the perturbation wavelength to be on the order of about 200 km.

[23] We also present TEC images derived from FR images for this case. Deriving TEC requires the specification of $\langle B \cos \theta \rangle$, which is computed using IGRF and the spacecraft attitude as well as observation geometry. Figure 7 shows examples of the $\langle B \cos \theta \rangle$ factor and TEC images derived from the third and fourth FR images (from left) shown in Figure 6. In these examples, $\langle B \cos \theta \rangle$ varies from 0.273

to 0.283 Gauss and TEC varies from 7.7 to 8.83 TECU (1 TECU = 10^{16} electrons/m²).

[24] This East Asia or west Pacific region is an interesting region where frequent activities of atmospheric gravity waves (AGWs) and traveling ionospheric disturbances have been reported [e.g., Saito *et al.*, 2001]. AGW is a phenomenon that perturbations in the atmosphere can propagate upward and horizontally owing to interplay of gravity and atmospheric buoyancy forces [e.g., Hines, 1964]. The atmospheric perturbations can be triggered by various possible sources, including (not limited to) earthquakes, tsunamis, and hurricanes. Some of these waves can penetrate into the thermosphere causing TIDs in the *F* region of the ionosphere.

[25] To investigate the perturbations seen in the SAR images, we have also examined GPS data collected using the GPS Earth Observation Network (GEONET) in Japan. GEONET stations have been installed all over Japan, and the network consists of more than 1200 stations. The average spacing of the GEONET stations is about 25 km. The GPS receivers at these stations are of dual-frequency geodetic survey type. TEC data derived from such GPS measurements are an excellent resource to compare with PALSAR images owing to the dense sampling. Examining the TEC measurements made using GEONET on the same day, we have identified southwest propagating TIDs occurred for at least a couple of hours during which ALOS passed over Japan when local time was about 2223 (ascending pass). Figure 8 shows an example of TEC perturbations observed using GEONET a few minutes before the ALOS pass. Further examining the GPS data, we notice that wave-like TEC perturbations in the entire region are on the order of 1 TECU (peak to trough). This corresponds to about 0.23 degrees in FR for the PALSAR measurements in this region. These values are close to but slightly smaller than the radar measurements shown in Figures 6 and 7. The differences seem to be due to the detrending done in the GPS TEC data while there is no detrending in the SAR data. This is verified after we remove the background trend on

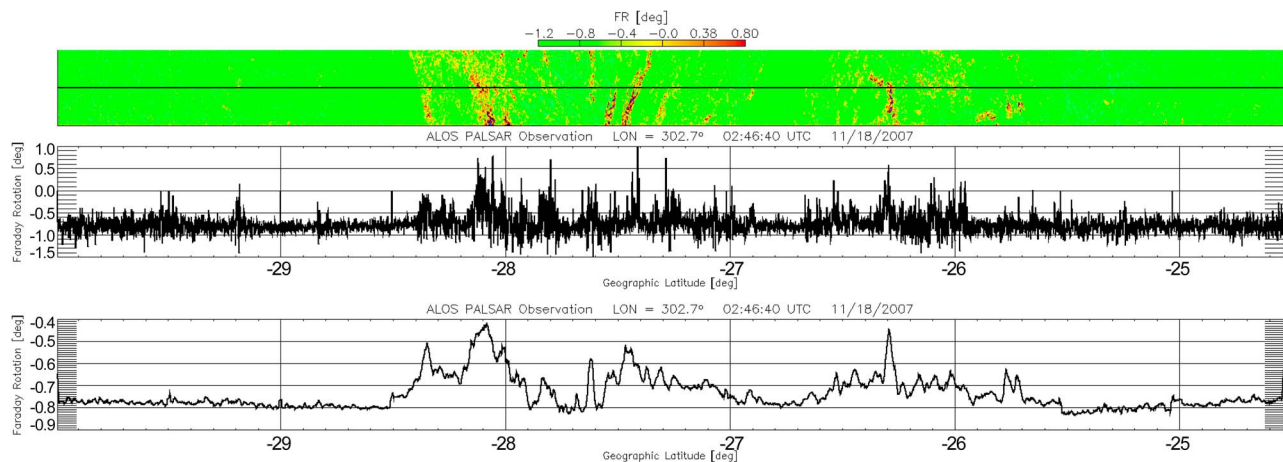


Figure 9. The 2- and 1-D line-of-sight Faraday rotation (FR) derived from polarimetric measurements made over Brazil on 18 November 2007 using PALSAR on board ALOS. The 1-D FR values are extracted from (middle) the center or (bottom) the average of the 2-D image. The data set shows a FR scintillation event associated with FR or TEC depletion that is captured in synthetic aperture radar images.

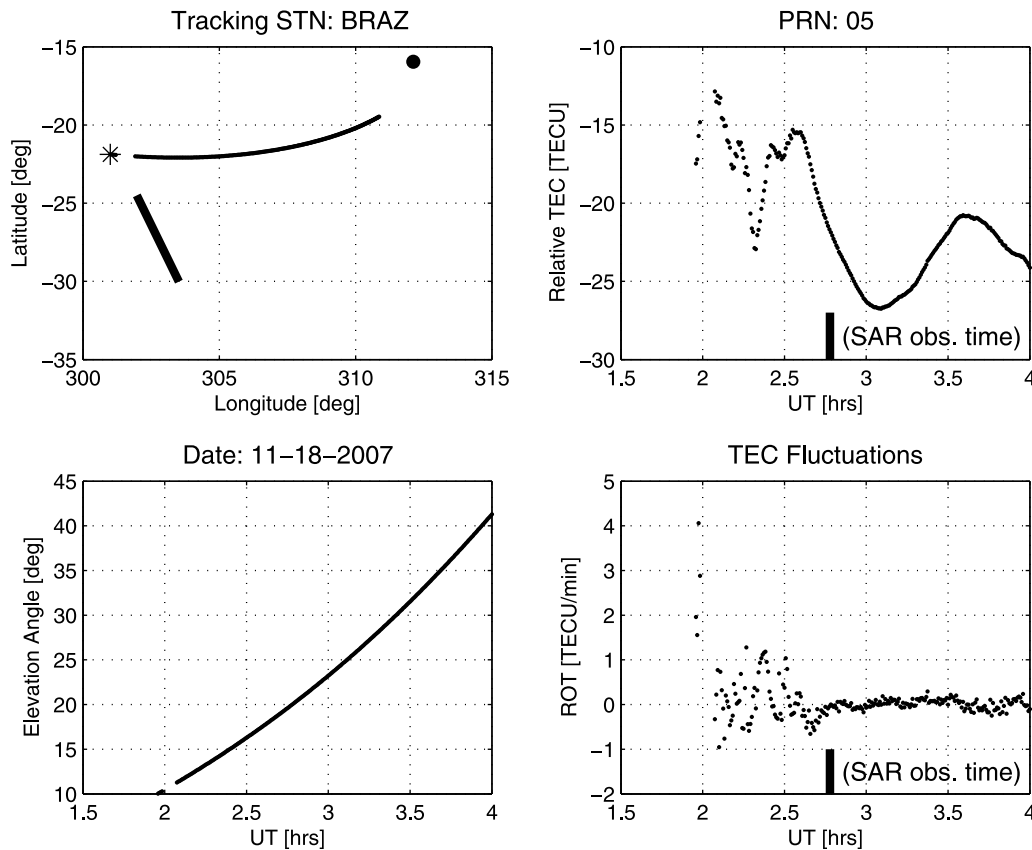


Figure 10a. Relative total electron content (TEC) and rate of TEC derived from GPS data collected from Brazil (15.95°S , 47.874°W). The observing site is marked by a large solid circle. The GPS observations on 18 November 2007 from receiver-to-satellite radio links (pseudorandom number (PRN) = 5) show perturbed TEC structures and TEC depletion in the region, as well as associated signal phase or TEC fluctuations (an indication of ionospheric irregularities). The asterisk indicates the starting point of the GPS track. The PALSAR observation track from lower to higher latitudes and the time of PALSAR observation are also marked (see Figure 1).

scales greater than 200 km in the SAR FR images. We would like to point out that although the stations of GEONET are very densely distributed, the network spatial resolution of TEC observations (~ 25 km) is incomparable with the spaceborne SAR (2 km to hundreds of meters), which makes detailed comparison difficult. Nevertheless the ground-based GPS network provides instantaneous or snapshot coverage over large regions. The two technologies nicely compensate each other and help to identify and reveal interesting ionospheric phenomena. In this case the phenomenon is TID.

4.4. Low-Latitude Plasma Bubbles and Irregularities

[26] Figure 9 shows PALSAR FR measurements for an ascending pass over Brazil on 18 November 2007. The 2-D FR images show irregular features between 25.5°S and 28.5°S geographic latitudes, which correspond to 14.8°S and 17.8°S invariant magnetic latitudes in the 57.3°W longitude sector. The FR values fluctuate randomly around -0.7° , as shown in Figure 9 (middle) in which FR values in the image center is plotted along the satellite orbit track (northward; see Figure 1d). In Figure 9 (bottom) the FR values averaged over the cross-track dimension are also

plotted along the satellite track. The mean values show overall depleted FR in regions where FR fluctuations are observed.

[27] We attribute the observed FR depletion and associated FR scintillation to ionospheric plasma bubbles and irregularities. The equatorial and low-latitude plasma bubbles often occur during evening from September through March in this longitude sector. These bubbles can be observed as electron density and TEC depletion. It is well understood through decades of studies that the occurrence of electron density irregularities in this region is associated with the evolution of plasma bubbles. The irregularities can cause amplitude, phase and polarization scintillation in radio signals propagating through them. The observed FR scintillation and depletion are good examples of such ionospheric effects on L band signals.

[28] To provide further evidence, we examined GPS data collected from the South America stations of the IGS network and found that there were significant ionospheric irregularity activities during the evening of interest. Figures 10a and 10b show examples of line-of-sight relative TEC and rate of TEC (ROT) derived from GPS data collected from the BRAZ station (15.95°S , 47.874°W). ROT or its index ROTI

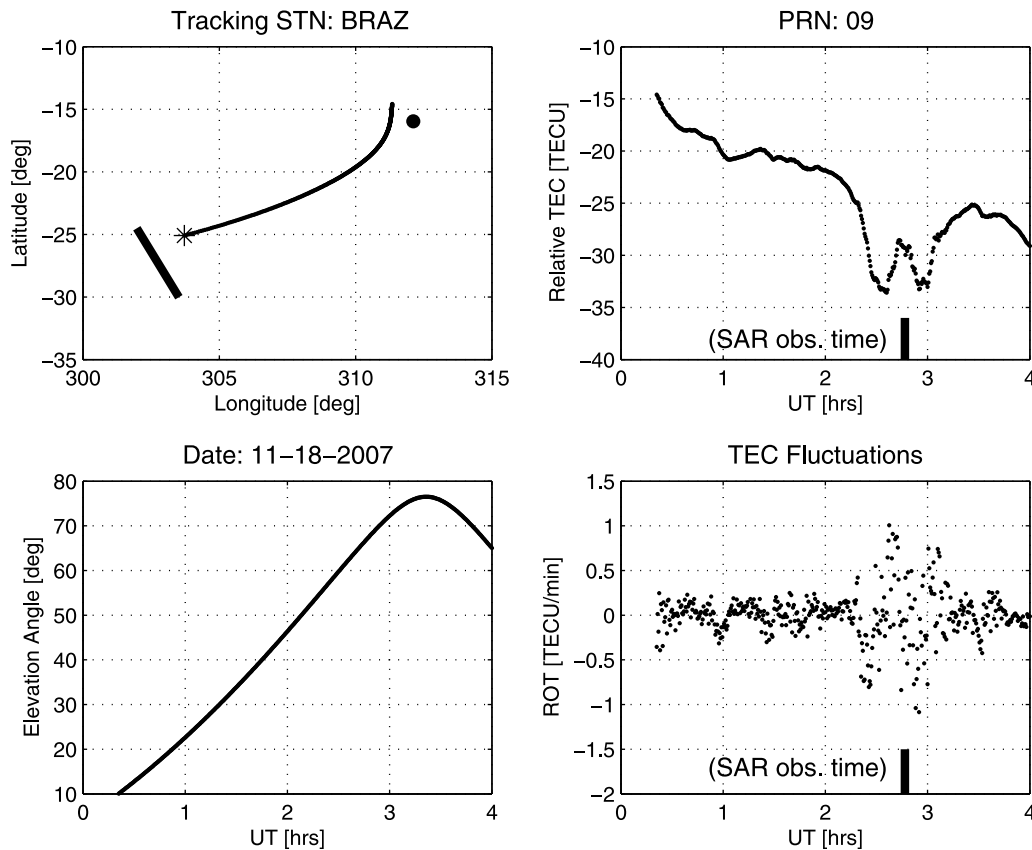


Figure 10b. Relative total electron content (TEC) and rate of TEC derived from GPS data collected from Brazil (15.95°S, 47.874°W). The observing site is marked by a large solid circle. The GPS observations on 18 November 2007 from receiver-to-satellite radio links (pseudorandom number (PRN) = 9) show perturbed TEC structures and TEC depletion in the region, as well as associated signal phase or TEC fluctuations (an indication of ionospheric irregularities). The asterisk indicates the starting point of the GPS track. The PALSAR observation track from lower to higher latitudes and time of PALSAR observation are also marked (see Figure 1).

measures GPS signal dual-frequency phase fluctuations and is an indicator of ionospheric irregularities [e.g., *Pi et al.*, 1997]. The measurements shown in Figures 10a and 10b are obtained by the receiver tracking two GPS satellites identified by the pseudorandom numbers (PRN5 and PRN9). Figure 10a shows TEC depletion and random fluctuations in ROT about half an hour earlier than the ALOS pass as the radio link to PRN5 satellite intercepted a region at the same longitude but at lower latitudes. As ALOS passed by at about 0247 UT, the GPS radio link to PRN9 satellite detected TEC depletion and ROT scintillation in a region a few degrees northeast of the ALOS pass as shown in Figure 10b. In fact, we also found TEC depletions and ROT fluctuations in other GPS radio links from the same receiver and other receivers of the network in the region. Although the GPS radio links do not precisely intercept the ALOS pass, we believe that the PALSAR measurements of plasma bubbles and FR scintillation are part of the ionospheric irregularity activities that occurred during that evening in the region. This assessment is partially based on the facts that the low-latitude plasma bubbles occur often in groups, they extend along the geomagnetic

flux tubes cross the magnetic equator and into both hemispheres, and they usually travel eastward in speed on the order of ~ 100 m/s. These characteristics have been published in many research works, and readers are referred to a readily accessible book for additional references [e.g., *Kelley*, 2009].

5. Image Resolutions

[29] The sampling spacing of PALSAR polarimetric SLC data is typically 9.369 and 3.557 m in range and azimuth (along-track) dimensions, respectively. The corresponding ground range spacing is about 23.128 m in the cross-track dimension. The spatial resolutions of a SAR FR image corresponding to the ground image size approximately depend on the number of radar looks that are used in smoothing or averaging to obtain the FR image. The resolutions are affected by the magnitude of FR or the FR signal-to-noise ratio. For example, if the surrounding 21×41 pixels in the range and azimuth dimensions are used in obtaining an averaged FR value for each pixel in order to reduce noise, the spatial resolutions would be about 486 and

146 m in cross- and along-track dimensions. In the case of PALSAR, the derived FR shows a level of background random noise at about 0.3° to 0.5° . Applying smoothing or averaging, we have obtained unambiguous images of aurora-associated ionospheric features with resolutions of about 0.5 km and 150 m in cross- and along-track dimensions, respectively, when FR values are a few degrees. In some cases, Earth topographic features can contaminate FR images. Minimizing such noises requires averaging with a large number of neighboring data points. In the TID case studied here, for example, the FR image resolution is reduced to about 2 km in each dimension in order to remove the noise introduced by topographic features in Japan. This resolution is fine enough for measuring appreciable medium-scale TIDs of which typical wavelengths are on the order of two to four hundred kilometers. We expect that higher resolutions of ionospheric imaging can be reached during active solar years when magnitude of ionospheric disturbances is greater than the solar minimum observations presented here.

6. Conclusions

[30] This study demonstrates a new technique for 2-D ionospheric imaging using a spaceborne *L* band polarimetric SAR system that is originally designed for land observations. It has been shown that 2-D Faraday rotation and TEC images can be derived from the polarimetric SAR data. We have shown that distinguished ionospheric inhomogeneities have been observed using the PALSAR on board the Japanese ALOS satellite. The observed phenomena include ionospheric enhancement arcs associated with aurora activities, FR or TEC gradient in the midlatitude trough region, midlatitude medium-scale TIDs, and plasma bubbles as well as associated polarization scintillation at low latitudes. The ionospheric perturbations observed by PALSAR are verified using ground-based GPS receivers and network, which provide measurements of TEC and irregularities near the regions of ALOS passes.

[31] Compared with other existing radio technologies, the ionospheric imaging using spaceborne SAR has great advantages, including: (1) 2-D images with relatively high spatial resolutions (subkilometers to kilometers), (2) global coverage, and (3) cost effectiveness, with one mission for both land and ionospheric observations. One disadvantage of the presented polarimetric approach is the need of full polarization measurements in four components (defined by polarization orientations of signal transmission and reception). This demands more sophisticated system than single or dual polarizations, and high-rate data downlink as well as large onboard storage. Using Tracking and Data Relay Satellite System (TDRSS, <http://esc.gsfc.nasa.gov/space-communications/tdrs.html>) and infrastructural upgrade of the ground segment, one could improve the data downlink significantly to accommodate the observation requirements. It is also desired to explore techniques that reduce the requirements of full polarization. Nevertheless we expect that SAR ionospheric imaging will become a great resource for future observations of ionospheric inhomogeneities and will also provide the required ionospheric correction to SAR and InSAR data for Earth observations.

[32] **Acknowledgments.** The authors thank the Japanese Aerospace and Exploration Agency, the Earth Observation Research Center of Japan, and Masanobu Shimada for providing PALSAR data for this study, and the Alaska Satellite Facility for processing and distributing PALSAR data. The authors also thank the International GNSS Service (IGS) for organizing the IGS GPS networking and archiving, as well as distributing the GPS data that are used in this study, and the Geographical Survey Institute of Japan and Akinori Saito at Kyoto University for providing the GEONET GPS TEC data for this study. The research performed at the Jet Propulsion Laboratory, California Institute of Technology, is under a contract with NASA.

[33] Robert Lysak thanks the reviewers for their assistance in evaluating this paper.

References

- Bickel, S. H., and R. H. T. Bates (1965), Effects of magneto-ionic propagation on the polarization scattering matrix, *Proc. IRE*, *53*, 1089–1091.
- Budden, K. G. (1985), *The Propagation of Radio Waves*, Cambridge Univ. Press, Cambridge, U. K.
- Chapin, E., S. F. Chan, B. D. Chapman, C. W. Chen, J. M. Martin, T. R. Michel, R. J. Muellerschoen, X. Pi, and P. A. Rosen (2006), Impact of the ionosphere on an L-band space based radar, paper presented at the 2006 IEEE Conference on Radar, Inst. of Electr. and Electron. Eng., Verona, N. Y., 24–27 April.
- Davis, K. (1990), *Ionospheric Radio*, Peter Peregrinus, London.
- Freeman, A. (2004), Calibration of linearly polarized polarimetric SAR data subject to Faraday rotation, *IEEE Trans. Geosci. Remote Sens.*, *42*, 1617–1624, doi:10.1109/TGRS.2004.830161.
- Freeman, A., X. Pi, B. Chapman, and E. Chapin (2008), Evaluation of GPS vs. polarimetric based approaches for correction of Faraday rotation in SAR data, paper presented at the 2008 IEEE International Geoscience and Remote Sensing Symposium, Inst. of Electr. and Electron. Eng., Boston, Mass.
- Freeman, A., X. Pi, and B. Chapman (2009), Calibration of PolSAR polarimetric data, paper presented at POLinSAR 2009, Eur. Space Agency, Esrin, Italy, 26 Jan.
- Hines, C. O. (1964), Internal atmospheric gravity waves at ionospheric heights, *Can. J. Phys.*, *38*, 1441–1481.
- Ishimaru, A., Y. Kuga, J. Liu, Y. Kim, and A. Freeman (1999), Ionospheric effects on synthetic aperture radar at 100 MHz to 2 GHz, *Radio Sci.*, *34*, 257–268, doi:10.1029/1998RS900021.
- Kelley, M. C. (2009), *The Earth's Ionosphere*, Academic, San Diego, Calif.
- Liszka, L. (1965), Variation according to latitude of the electron content of the ionosphere near the auroral zone, *Nature*, *208*, 280–281, doi:10.1038/208280a0.
- Liu, J., Y. Kuga, A. Ishimaru, X. Pi, and A. Freeman (2003), Ionospheric effects on SAR imaging: A numerical study, *IEEE Trans. Geosci. Remote Sens.*, *41*, 939–947, doi:10.1109/TGRS.2003.811813.
- Meyer, F., and J. Nicoll (2008), Ionospheric effects on SAR, InSAR, and SAR polarimetry—Theory and experiences with ALOS/PALSAR, paper presented at the 2008 IEEE International Geoscience and Remote Sensing Symposium, Inst. of Electr. and Electron. Eng., Boston, Mass.
- Muldrew, D. B. (1965), *F* layer ionization troughs deduced from Alouette data, *J. Geophys. Res.*, *70*, 2635–2650, doi:10.1029/JZ070i011p02635.
- Pi, X., and S. Chan (2006), Effects of polar ionospheric scintillation on L-band space-based radar, *Tech. Rep.*, Jet Propul. Lab., Pasadena, Calif.
- Pi, X., A. J. Mannucci, U. J. Lindqwister, and C. M. Ho (1997), Monitoring of global ionospheric irregularities using the Worldwide GPS Network, *Geophys. Res. Lett.*, *24*, 2283–2286, doi:10.1029/97GL02273.
- Pi, X., A. Freeman, B. Chapman, and E. Chapin (2008), Imaging the ionosphere using polarimetric SAR and GPS, *Eos Trans. AGU*, *89*(53), Fall Meet. Suppl., Abstract G51C-04.
- Quegan, S. (1994), A unified algorithm for phase and cross-talk calibration of polarimetric data—Theory and observations, *IEEE Trans. Geosci. Remote Sens.*, *32*, 89–99, doi:10.1109/36.285192.
- Rosen, P., E. Chapin, C. Chen, S. Hensley, and X. Pi (2009), Ionosphere effects in polarimetric and interferometric SAR imagery, paper presented at the 2009 IEEE International Geoscience and Remote Sensing Symposium, Inst. of Electr. and Electron. Eng., Cape Town, South Africa.
- Saito, A., et al. (2001), Traveling ionospheric disturbances detected in the FRONT Campaign, *Geophys. Res. Lett.*, *28*, 689–692, doi:10.1029/2000GL011884.
- Schunk, R. W., W. J. Raitt, and P. M. Banks (1975), Effect of electric fields on the daytime high-latitude *E* and *F* regions, *J. Geophys. Res.*, *80*, 3121–3130, doi:10.1029/JA080i022p03121.
- Shimada, M., Y. Muraki, and Y. Otsuka (2008), Discovery of anomalous stripes over the Amazon by the PALSAR onboard ALOS satellite, paper

presented at the 2008 IEEE International Geoscience and Remote Sensing Symposium, Inst. of Electr. and Electron. Eng., Boston, Mass.
Shimada, M., O. Isoguchi, T. Tadono, and K. Isono (2009), PALSAR radiometric and geometric calibration, *IEEE Trans. Geosci. Remote Sens.*, *47*, 3915–3932.

Spiro, R. W., R. A. Heelis, and W. B. Hanson (1978), Ion convection and the formation of the P90, midlatitude *F* region ionization trough, *J. Geophys. Res.*, *83*, 4255–4264, doi:10.1029/JA083iA09p04255.

B. Chapman, A. Freeman, X. Pi, and P. Rosen, Jet Propulsion Laboratory, California Institute of Technology, M/S 138-308, 4800 Oak Grove Dr., Pasadena, CA 91109, USA. (xiaoqing.pi@jpl.nasa.gov)

Z. Li, Department of Geographical and Earth Sciences, University of Glasgow, Glasgow G12 8QQ, UK.